Available online at www.sciencedirect.com

ScienceDirect

Journal of the European Ceramic Society 30 (2010) 677–688

www.elsevier.com/locate/jeurceramsoc

Onset coarsening/coalescence of cobalt oxides in the form of nanoplates versus equi-axed micron particles

Yichi Yeh, I.-Hsien Liu, Pouyan Shen*

Institute of Materials Science and Engineering, Department of Materials and Optoelectronic Science,
National Sun Yat-sen University, Kaohsiung, Taiwan, ROC

Received 26 June 2009; received in revised form 1 September 2009; accepted 5 September 2009
Available online 30 September 2009

Abstract

The change of specific surface area and pore size distribution coupled with N_2 adsorption–desorption hysteresis isotherm, in particular that typical to cylindrical pores, were used to determine the onset coarsening/coalescence in the temperature range of 500–800 °C for $Co(OH)_2$ derived Co_3O_4 nanoplates and 700–1000 °C for CoO-derived Co_3O_4 powders (backtransformed to CoO above 900 °C) which are equi-axed in shape and microns in size. The vigorous onset coarsening/coalescence of the nanoplates and equi-axed micron particles was found to occur within minutes having apparent activation energy of 37 ± 7 kJ/mol (based on $t_{0.7}$, i.e. time for 70% surface area reduction) and 113 ± 8 kJ/mol (based on $t_{0.3}$), respectively. The surface area reduction process of the nanoplates was found to be controlled by (1 1 1)-specific coalescence besides a coarsening–repacking process more common to the equi-axed particles. The present static experimental results of coarsening–coalescence of the Co_3O_4 (below 900 °C) or CoO particles (above 900 °C) supports our previous supposition that CoO and Co_3O_4 nanocondensates could readily assemble as nanochain aggregates and further coalesce into a close packed manner below 1000 °C by the radiant heating effect in a dynamic laser ablation process.

Keywords: Onset coarsening–coalescence; Co_3O_4; Precursor; Size; Shape; BET; TEM

1. Introduction

Cobalt oxides have important heterogeneous catalysis applications like other semiconductors.[1,2] The criteria for an industrially successful catalyst are surface activity and durability in a specified temperature and pressure range.[2] Irreversible physical changes, such as loss of surface area upon thermal exposure, are thus of concern to the preparation and catalysis use of cobalt oxides.

Thermally activated phase behavior of cobalt oxide has been extensively studied by static heating experiments of sintered powders with or without the presence of dopant or second phase, such as that focusing on interdiffusion induced defect clustering,[3–6] reorientation of intra- and intergranular particles,[7–9] thermal mismatch- or transformation-enabled cleaving-healing of the host lattice[10,11] and surface morphology due to directional dislocation exposure and $Co_{1-x}O$ condensation.[12]

The phase behavior of cobalt oxides via a dynamic laser process was also reported regarding the deposition of $Cr_{3-\delta}O_4$ spinel particles upon laser heated pedestal growth of Cr:YAG fiber[13] and laser ablation condensation and phase change of $Ni_{1-x}Co_xO$ nanoparticles agglomerated in nanochain aggregates or a more close packed manner due to pulsed radiant heating.[14] Such a radiant heating is presumably up to 1000 °C in order to activate the sintering process of nanoparticles analogous to that suggested for the TiO_2 nanocondensates prepared by gas evaporation.[15] The thermally activated competition of onset sintering and coarsening/coalescence of cobalt oxides, however, remained to be studied more carefully.

Recently a vigorous onset coarsening–coalescence event of γ-type related Al_2O_3 with a mean particle diameter of 10 and 50 nm was found to cause cylindrical mesopore formation with an accompanied significant change of specific surface area.[16] Such a static heating result sheds light on size dependent surface state and hence surface diffusion-controlled

---

* Corresponding author.
E-mail address: pshen@mail.nsysu.edu.tw (P. Shen).

0955-2219/$ – see front matter © 2009 Elsevier Ltd. All rights reserved.
doi:10.1016/j.jeurceramsoc.2009.09.004

coarsening–coalescence of alumina in a dynamic laser ablation process.[17]

Here we report further the size and shape dependent onset coarsening–coalescence kinetics of Co_3O_4 powders upon a rather short static thermal exposure in air. There are several research problems we intended to solve. First, to prove that the static heating and specific surface area measurement techniques used in our previous study of onset coarsening/coalescence of γ-Al_2O_3 particles[16] can be extended to other ceramic systems. Second, to clarify whether the Co_3O_4 nanoparticles lose surface area at temperatures much lower than the refractory γ-Al_2O_3 nanoparticles with a spinel-type isostructure.[16] Third, to focus on the surface area reduction of the Co_3O_4 nanoplates involving $\{1\,1\,1\}$-specific coalescence besides a coarsening–repacking process more common to the equi-axed particles. The present experimental results also shed light on the phase behavior of cobalt oxide nanoparticles in a dynamic radiant heating process.[14]

2. Experimental

Powdery $Co(OH)_2$ (Sinoxp, 99.5% pure) and CoO (Aldrich, 99.9% pure) less than 100 nm and 0.5 μm in particle diameter, respectively were die-pressed at 650 MPa into disks ca. 5 mm in diameter and 2 mm in thickness. The two powders were dispersed on a carbon-coated collodion film for phase, shape and size distribution characterizations using transmission electron microscopy (TEM, JEOL3010 at 300 kV). Such dry pressed powders were used as the precursors of nanosized and micron-sized Co_3O_4 for isothermal firing in the temperature range of 500–800 and 700–1000 °C, respectively for specified time period up to 1 h in an open air furnace. Microstructure changes of the samples due to dry pressing and heating were studied by scanning electron microscopy (SEM, JEOL 6330 at 20 kV). The phase identity of the dry pressed and heated samples was also determined by X-ray diffraction (XRD, Cu Kα, 40 kV, 30 mA at 0.05° and 3 s per step).

Nitrogen adsorption/desorption isotherms of the dry pressed and then heated powders were conducted at liquid nitrogen temperature of 77 K using a Micromeritics ASAP 2020 instrument. The surface area and pore size distributions were obtained from the N_2 adsorption and desorption branch, using the Brunauer–Emmett–Teller (BET) method[18] and Barrett–Joyner–Halenda (BJH) method,[19] respectively. The BET isotherm and BJH adsorption/desorption hysteresis type of the samples are classified according to the scheme of International Union of Pure and Applied Chemistry (IUPAC).[20] The H1 type adsorption/desorption hysteresis loop of the type IV isotherm (Appendix 1) was used as an indicator of cylindrical pore formation and onset sintering.

3. Results

3.1. Phase identity of the dry pressed powders upon heating

The phase identity of the dry pressed powders upon heating were determined by XRD and compiled in Tables 1 and 2 for the nanosized and micron-sized powders, respectively. The representative XRD traces indicated that the starting nanosized $Co(OH)_2$ powders (Fig. 1a) were transformed into spinel-type Co_3O_4 after firing, e.g. at 700 °C for 4 min, in air (Fig. 1b). The micron-sized CoO powders with rock salt type structure (Fig. 1c)

Table 1
BET/BJH data and phase identity of nanosize $Co(OH)_2$ derived Co_3O_4 powder subjected to various treatments.

T (°C)–*t* (min)	Specific surface area (m^2/g)	Ads./desorp. pore width (nm)	Phases
Dry pressed[a]	106.94 (S_0)	5.6/5.1	sp $\gg$ r
500–1	125.65	5.9/5.5	sp
500–5	25.25	22.5/17.9	sp
500–10	21.25	22.2/18.9	sp
500–30	20.17	23.9/19.7	sp
500–50	17.90	26.5/21.7	sp
500–60	17.15	28.2/22.9	sp
600–0.5	101.78	6.0/5.5	sp
600–1	119.35	5.5/5.1	sp
600–5	19.52	26.5/22.2	sp
600–10	13.56	32.0/26.5	sp
600–20	13.66	26.9/24.4	sp
600–50	12.48	28.7/26.6	sp
600–60	6.24	30.9/28.1	sp
700–0.5	104.72	6.3/5.8	sp
700–1	70.69	8.7/7.5	sp
700–3	20.43	19.7/16.9	sp
700–4	12.60	24.4/22.5	sp
700–5	10.46	24.9/23.1	sp
700–10	9.18	25.9/24.2	sp
800–0.5	121.09	6.1/5.6	sp
800–1	26.55	18.3/15.6	sp
800–2	19.33	20.4/18.3	sp
800–3	7.05	27.0/23.4	sp
800–4	7.86	12.0/11.1	sp

[a] Degassed at 300 °C.

Table 2
BET/BJH data and phase identity of micronsize CoO-derived Co_3O_4 powder subjected to various treatments.

T (°C)–*t* (min)	Specific surface area (m^2/g)	Ads./desorp. pore width (nm)	Phases
Dry pressed[a]	6.59 (S_0)	55.4/39.8	sp $\gg$ r
700–10	5.97	15.0/14.6	sp
700–30	4.24	16.4/11.4	sp
700–53	3.72	18.3/21.5	sp
700–60	3.69	19.9/21.7	sp
800–7	4.98	47.9/36.9	sp
800–9	3.89	18.37/16.66	sp
800–10	3.91	29.9/22.3	sp
800–12	3.63	34.5/30.4	sp
900–2	5.00	45.4/35.0	sp
900–3	4.23	33.2/25.7	sp
900–4	4.92	28.0/26.9	sp
900–6	3.95	37.3/34.5	sp
1000–1	4.33	26.3/22.0	sp[b]
1000–2	3.12	40.7/34.5	sp[b]
1000–3	4.00	32.9/31.5	sp[b]
1000–4	2.64	21.3/33.7	sp[b]

[a] Degassed at 300 °C.

[b] The Co_3O_4 becomes CoO at 1000 °C according to Ref. 25, which backtransformed to the spinel phase when cooled in an open air furnace.

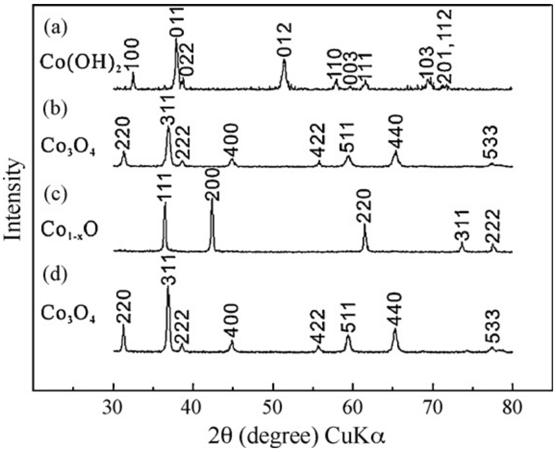

Fig. 1. XRD traces (Cu Kα) of (a) starting $Co(OH)_2$ nanometers in size, (b) spinel-type Co_3O_4 nanoparticles derived from $Co(OH)_2$ by firing at 700 °C for 4 min in air, (c) starting rock salt type CoO micrometers in size, and (d) micron-sized Co_3O_4 powders derived from CoO by firing at 800 °C for 3 min in air.

were also transformed into spinel-type Co_3O_4 after firing, e.g. at 800 °C for 3 min in air (Fig. 1d).

3.2. *Shape of the starting powders*

TEM bright field image (BFI) (Fig. 2a) and corresponding SAED pattern coupled with schematic indexing (Fig. 2c) further showed that the starting $Co(OH)_2$ hydride (denoted as H) nanoparticles are hexagonal plate-like with well-developed (0 0 0 1) and $\{1 0 \bar{1} 0\}$ surfaces, which were partially decomposed as a single-(1 1 1) faceted Co_3O_4 spinel (denoted as S) and Co following a specific crystallographic relationship, $[0 0 0 1]_H//[1 1 1]_S//[0 0 0 1]_{Co}$; $(1 0 \bar{1} 0)_H//(\bar{1} \bar{1} 2)_S//(\bar{1} \bar{1} 2 0)_{Co}$. Further electron dosage forced the $Co(OH)_2$ to transform further into Co_3O_4 and Co (Fig. 2d). This transformation scheme is analogous to the NiO pseudomorph after $Ni(OH)_2$,[21] and the thermal decomposition of $Co(OH)_2$ to form CoO and then Co_3O_4 in the temperature range 80–180 °C under ambient air conditions.[22]

The plate-like Co_3O_4 nanoparticles derived from $Co(OH)_2$ by electron irradiation kept the shape and were commonly in agglomeration (Fig. 3a). The SAED pattern (Fig. 3b) and lattice image (Fig. 3c) of a representative nanoparticle in $[2 \bar{1} 1]$ zone axis showed cubo-octahedra mesopores regardless of the external hexagonal shape of the particle. The 2D inverse Fourier transform (Fig. 3d) further showed the presence of dislocations with half plane parallel to $(1 1 \bar{1})$ for the plate-like Co_3O_4 nanoparticle with composition confirmed by point count EDX spectrum (Fig. 3e). Such Co_3O_4 nanoplates preferred to attach on their single (1 1 1) surface to form variants off by 30° (Fig. 4).

The micron-sized CoO powders were almost equi-axed (Fig. 5a) which were agglomerated in random orientation as

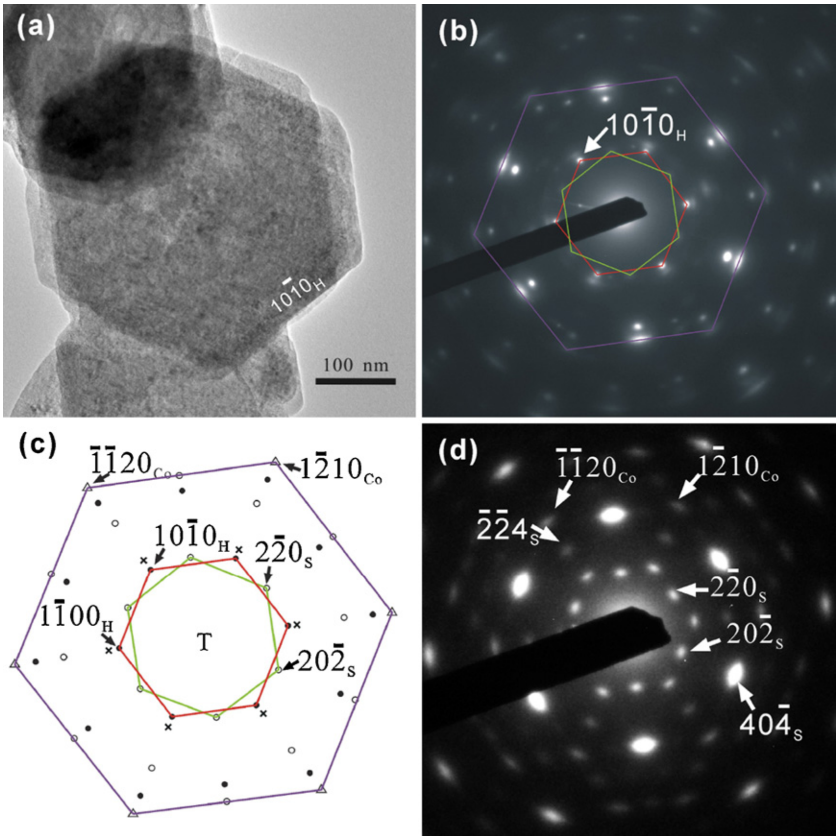

Fig. 2. TEM (a) BFI of plate-like $Co(OH)_2$ nanoparticle with well-developed (0 0 0 1) and $\{1\ 0 \bar{1} 0\}$ surfaces, (b) corresponding SAED pattern with schematic indexing in (c) showing the diffractions of $Co(OH)_2$ (closed circle, denoted as H), Co_3O_4 (open circle, denoted as s) and Co (triangle) in epitaxial relationship $[0 0 0 1]_H//[1 1 1]_S//[0 0 0 1]_{Co}$; $(1\ 0 \bar{1} 0)_H//(\bar{1} \bar{1} 2)_S//(\bar{1} \bar{1} 2 0)_{Co}$. Note double diffractions denoted as crosses. (d) $Co(OH)_2$ further transformed into Co_3O_4 and Co upon further electron dosage.

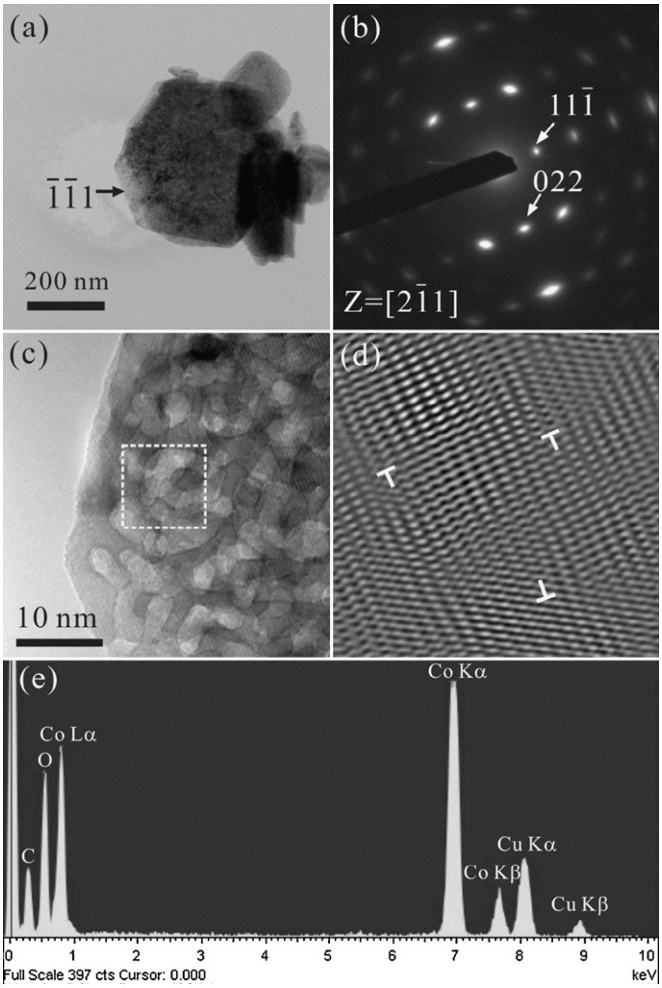

Fig. 3. TEM (a) BFI of plate-like Co_3O_4 nanoparticles in agglomeration which were pseudomorph after $Co(OH)_2$ by electron irradiation, (b) and (c) corresponding SAED pattern and lattice image in $[2\ \bar{1}\ 1]$ zone axis for the nearly hexagonal shaped particle in (a) showing cubo-octahedral mesopores regardless of the hexagonal shape of the plate-like particle, (d) inverse Fourier transform from the square region in (c) showing dislocations with half plane parallel to $(1\ 1\ \bar{1})$, (e) point count EDX spectrum showing Co and O counts for the plate-like Co_3O_4 nanoparticle having C and Cu counts from supporting film and specimen holder, respectively.

indicated by ring diffractions (Fig. 5b). These powders remained as rock salt type structure during TEM observations, but transformed into Co_3O_4 spinel when fired at temperatures in open air according to the XRD results compiled in Table 2.

3.3. *Specific surface area, pore and microstructure changes upon heating*

BET data of the fired samples indicated that the specific surface area decreases whereas average pore size increases with the increase of dwelling time at a specific firing temperature for both nano- and micron-sized Co_3O_4 powders as compiled in Tables 1 and 2, respectively. The drastic change of specific surface area and average pore size are related to the formation of cylindrical and/or truncated pores as further revealed by the following BJH analyses.

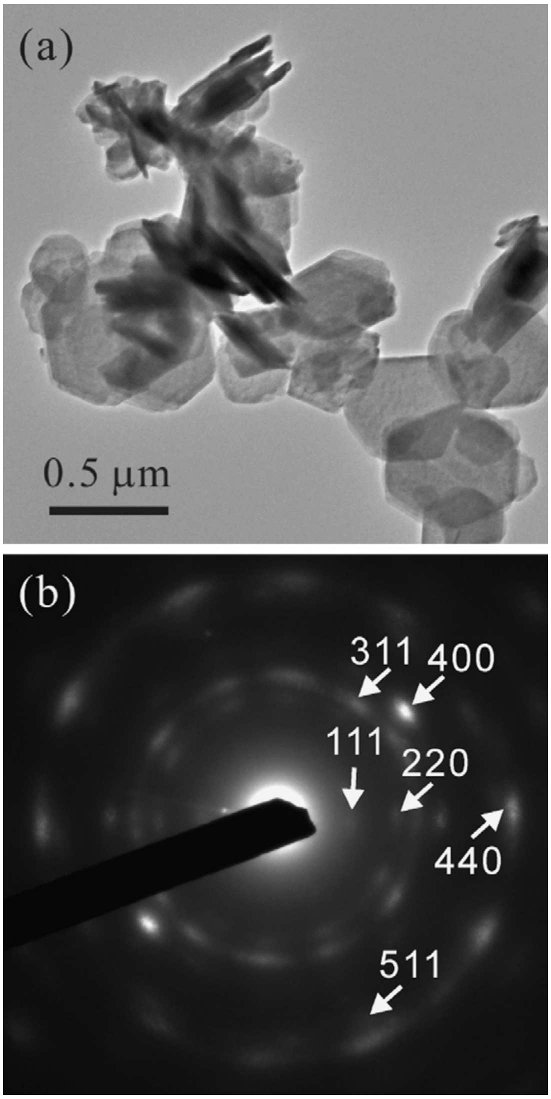

Fig. 4. (a) TEM BFI and (b) corresponding SAED pattern of a number of plate-like $Co(OH)_2$ ([0 0 0 1] oriented) nanoplates which transformed upon electron irradiation into [1 1 1] oriented Co_3O_4 variants with neighboring {2 2 0} diffraction arcs off by 30°.

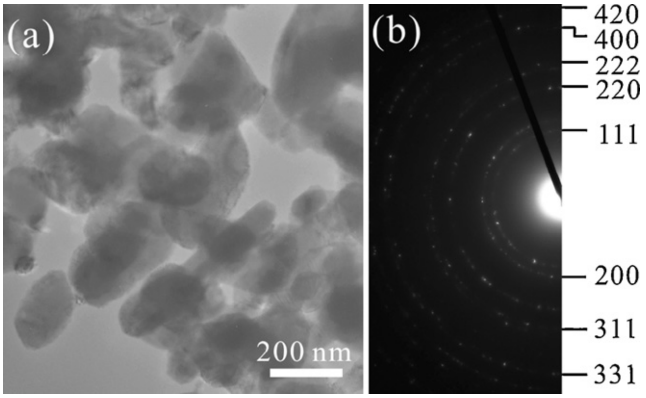

Fig. 5. TEM (a) BFI and (b) SAED of micron-sized CoO powders in random orientation as indicated by ring diffractions indexed according to rock salt type structure.

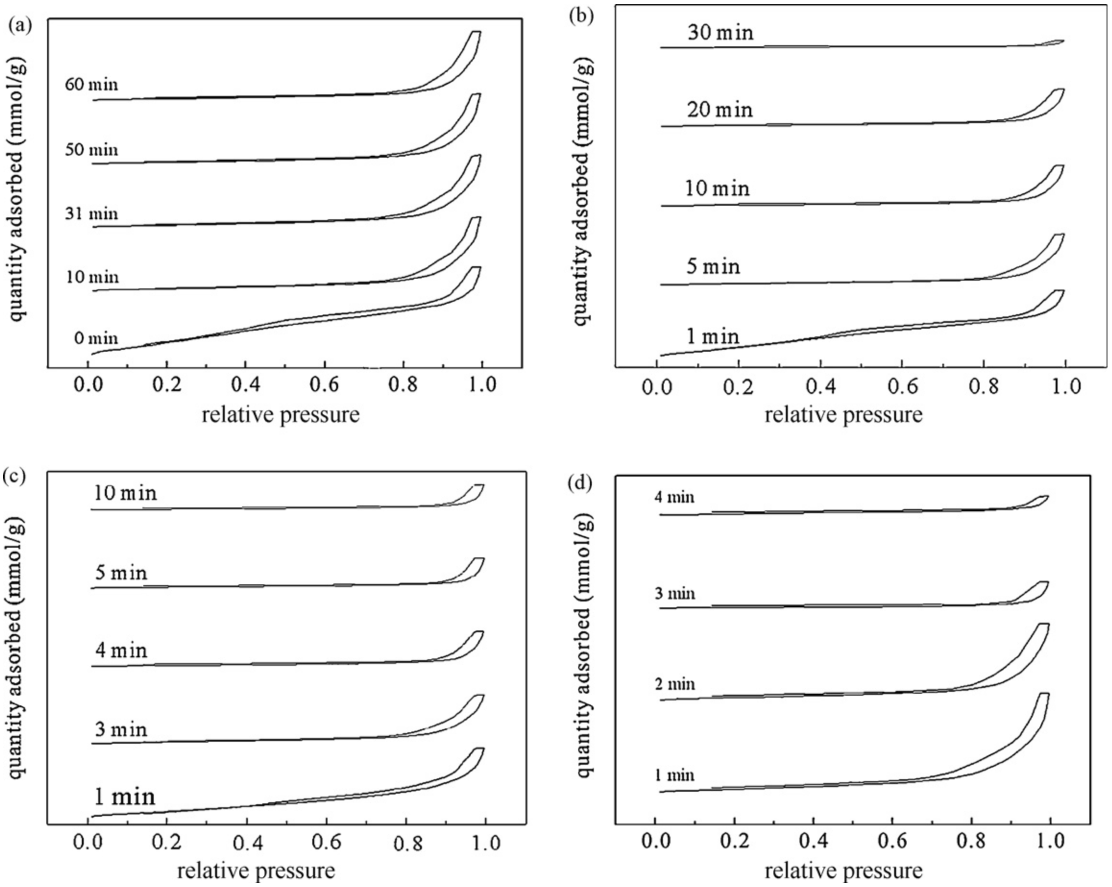

Fig. 6. BJH N_2 adsorption–desorption hysteresis isotherms for the dry pressed nanosized powders fired at various conditions: (a) 500 °C for 0–60 min, (b) 600 °C for 1–30 min, (c) 700 °C for 1–10 min, and (d) 800 °C for 1–4 min.

The BJH N_2 adsorption–desorption hysteresis isotherms for the nanosized Co_3O_4 powders dry pressed and further fired at 500, 600, 700 and 800 °C for specified time periods are shown in Fig. 6a–d, respectively. The green body consisting of such sized powders shows a H4 type loop in the relative pressure range 0.4–1.0, which is characteristic of narrow slit-like pores.[20] This indicates a nanosize effect on the surface state of the powders as discussed later. The loop shifts to a higher relative pressure and changes into H1 type corresponding to cylindrical pores, e.g. for the samples fired for ca. 10 min at 500 °C (Fig. 6a) and for a shorter time at higher temperatures (Fig. 6b–d). Considering further a more drastic decrease (70%) of the specific surface area relative to the dry pressed sample (Table 1, cf. rate curves in Appendix 2) than the case of micron-sized samples (Table 2, cf. rate curves in Appendix 3), the onset time $t_{0.7}$, i.e. for a total of 70% drop of the specific surface area and accompanied cylindrical pore formation, in the nanosized samples was determined as 5 ± 1, 4 ± 0.5, 2 ± 0.3 and 1 ± 0.2 min for 500, 600, 700 and 800 °C, respectively. A longer firing time in this temperature range improves the H1 type loop, presumably due to repacking of the nanosized powders as discussed later, and shifts it toward a higher relative pressure 0.9–1.0, as indicated by the samples fired beyond 30 min at 600 °C (Fig. 6b), 5 min at 700 °C (Fig. 6c) and 3 min at 800 °C (Fig. 6d).

The BJH N_2 adsorption–desorption hysteresis isotherms for the micron-sized Co_3O_4 powders dry pressed and further fired at 700, 800, 900 and 1000 °C for specified time periods are shown in Fig. 7a–d, respectively. As shown in Fig. 7a, the hysteresis loop is already H1 type (Appendix 1) for the dry pressed sample. There is a significant decrease of the specific surface area with respect to the dry pressed sample (Table 2, cf. rate curves in Appendix 3), which corresponds to a steady coarsening–coalescence process as discussed later. In general, the hysteresis loops are in the relative pressure range 0.9 and 1.0 (i.e. actual pressure range 684–760 mmHg) for these samples. The time for a significant decrease of specific surface area with respect to the dry pressed sample by ~30% decreases with the increase of firing temperature, i.e. 27 ± 3, 7.5 ± 1, 2.5 ± 0.3 and 1 ± 0.2 min at 700, 800, 900 and 1000 °C, respectively (Fig. 7a–d). A longer firing time in this temperature range caused the change of H1 type loop into irregular shape, presumably due to the formation of the truncated pores from cylindrical ones. In general, such a deteriorating loop shifts toward a higher relative pressure 0.95–1.0, i.e. actual pressure range 722–760 mmHg as indicated by the samples fired beyond 10 min at 700 °C (Fig. 7a), beyond 9 and 6 min at 800 and 900 °C (Fig. 7b and c, respectively), and beyond 1 min at 1000 °C (Fig. 7d).

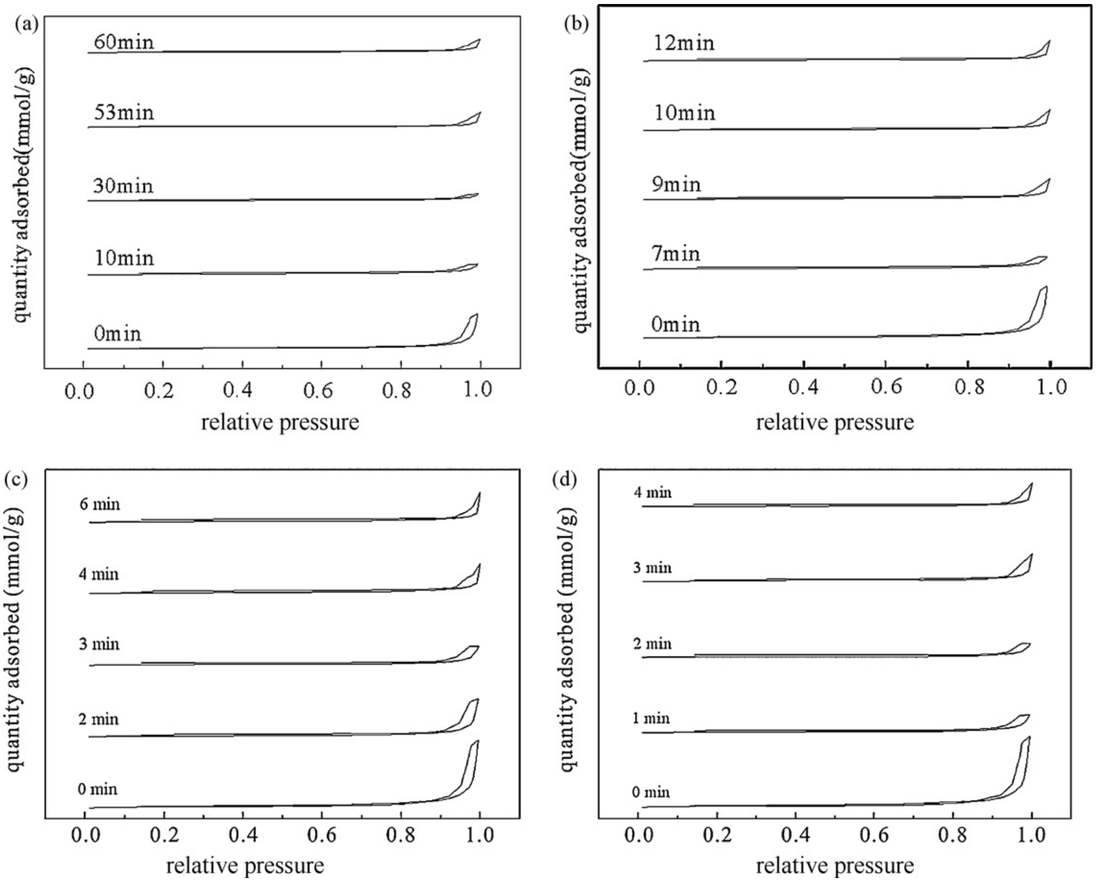

Fig. 7. BJH N_2 adsorption–desorption hysteresis isotherms for the dry pressed micron-sized powders fired at various conditions: (a) 700 °C for 0–60 min, (b) 800 °C for 0–12 min, (c) 900 °C for 0–6 min, and (d) 1000 °C for 0–4 min.

3.4. SEM observations of dry pressed and further heated samples

In general, dry pressing did not cause appreciable cracking and particle size change but cause significant agglomeration for the finer sized particles as indicated by SEM secondary electron images of the two samples with different average particle size in Figs. 8a and 9a. In fact, the dry pressed nanosize powder with hexagonal plate-like shape showed varied size and shape of pores among the particles with preferred orientation (Fig. 8a). TEM observations of the sample fired at 600 °C for 10 min further showed that the Co_3O_4 spinel plates were significantly coarsened/coalesced and the mesopores within the single crystal were also coarsened/coalesced (Fig. 10). By contrast, the sample dry pressed with an average particle diameter of micron size has relatively uniform pore size at grain corners (Fig. 9a). In both cases, the cylindrical pores characteristic of slightly sintered bodies are vague, and the relative density is difficult, if not impossible, to measure because the dry pressed powders tended to disperse in water during such measurements.

The presence of cylindrical and truncated pores, an indicator of onset and further coarsening/coalescence or even sintering, in the samples fired for a suitable time period at a specified temperature was confirmed by SEM observations, as shown in Figs. 8 and 9, for the case of nano- and micron-sized powders, respectively. Significant repacking and coalescence of slightly coarsened particles was observed to be associated with the sintering process in particular for the finer particles as circled in a magnified image in Fig. 9c.

4. Discussion

4.1. Adsorption–desorption hysteresis loop characteristic of cylindrical mesopores

Capillary condensation typically occurs for mesopores in a size range 2–50 nm to show type IV isotherm (Appendix 1a), which can be classified into H1 to H4 subtypes (Appendix 1b). According to the present observations of BJH N_2 adsorption–desorption isotherms, the dry pressed samples with predominant Co_3O_4 via degassing before BET/BJH measurements have a hysteresis loop somewhat between H1 and H2 type when prepared from micron-sized powders, whereas a H4 type corresponding to narrow slit-like pores[20] when prepared from the nm-sized powders having an average pore size (ca. 5 nm, Table 1) one order-of-magnitude smaller than that of the former (ca. 48 nm, Table 2).

Regardless of the difference in powder size, those Co_3O_4 samples just went through an onset coarsening–coalescence

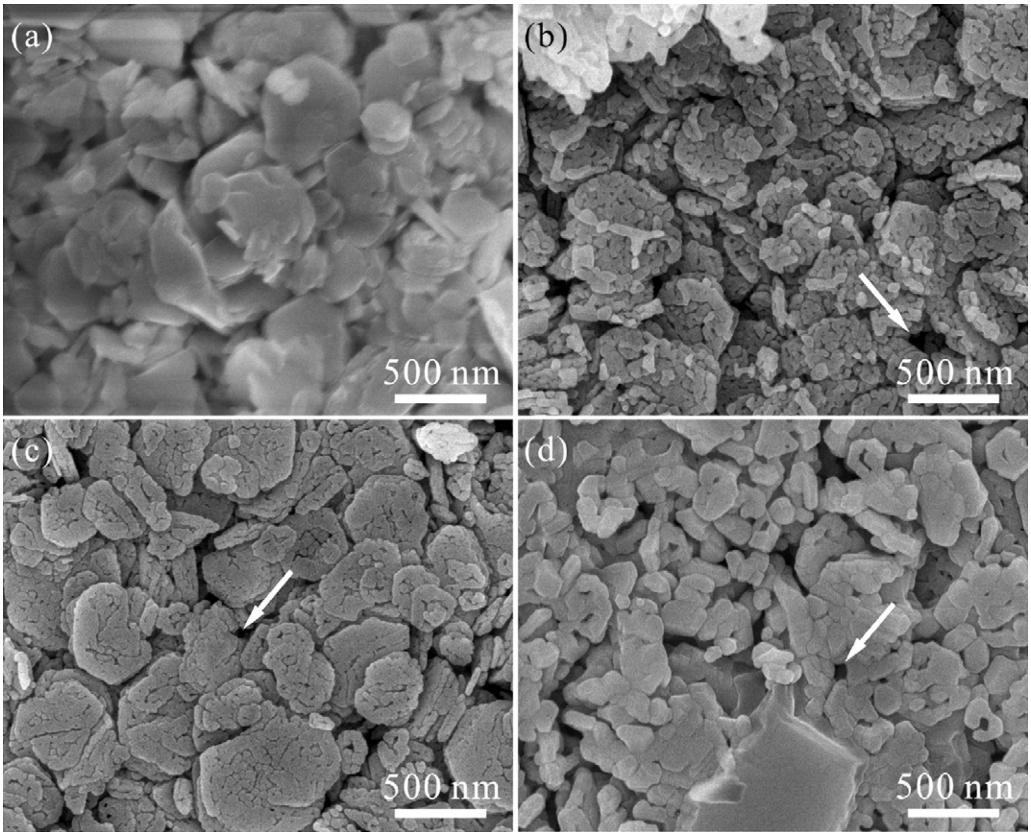

Fig. 8. Representative SEM images of nanosized powders: (a) dry pressed green body, (b), (c) and (d) subjected to sintering at 500 °C for 60 min, 600 °C for 10 and 20 min, respectively to show cylindrical pores (arrow) in (b) and (c) and isolated pores (arrow) in (d).

event have cylindrical mesopores with a characteristic H1 type hysteresis loop similar to the case of other mesoporous materials with a pore width range 2–50 nm.[20] The kinetics to form cylindrical mesopores, however, depend on the size of the starting powders. Having a smaller pore size, the sample composed of nm- rather than micron-sized powders would promote pore migration and growth/coalescence at high temperatures. This accounts for a wider size distribution of pores and less well defined H1 type loop in a wider range of relative pressure for the nm- than the micron-sized powders upon firing. A longer firing time (beyond 10 min) at 700 °C improved but smeared the H1 type loop for the samples composed nm- and micron-sized powders, respectively. This can be attributed to a more pronounced coarsening and repacking process of nanoparticles for effective sintering (cf. Fig. 7 of Ref. 23) and cylindrical pore formation, whereas necking of the cylindrical pores to form truncated pores for the sample composed of larger sized powders. Alternatively surface energy change due to size reduction and/or shape specification of the Co_3O_4 particles may affect the kinetics of N_2 adsorption and desorption and hence the hysteresis loop.

4.2. Activation energy and mechanism of onset coarsening–coalescence

On the basis of the appearance of the adsorption–desorption hysteresis loop characteristic of cylindrical mesopores and the drastic decrease of specific surface area by 70% (Table 1) in the linear region of the rate curves (Appendix 2), the onset time $t_{0.7}$ for nanosize Co_3O_4 powders to coarsen and coalesce was determined as 5 ± 1, 4 ± 0.5, 2 ± 0.3 and 1 ± 0.2 min at 500, 600, 700 and 800 °C, respectively. The corresponding Arrhenius plot of the reciprocal time $t_{0.7}$ for onset coarsening–coalescence versus the reciprocal temperature in Kelvin gives an apparent activation energy 37 ± 7 kJ/mol considering the maximum uncertainty of each data point (Fig. 11a). As a comparison, the micron-sized powders have higher activation energy (113 ± 8 kJ/mol) for onset coarsening–coalescence given the Arrhenius plot of the data points 27 ± 3, 7.5 ± 1, 2.5 ± 0.3 and 1 ± 0.2 min, i.e. $t_{0.3}$ for a less drastic decrease of specific surface area by 30% (Appendix 3) at 700, 800, 900 and 1000 °C, respectively in Fig. 11b. It is noteworthy that the apparent activation energy of a rapid onset coarsening–coalescence event is higher for more refractory γ-Al_2O_3 (119 ± 19 and 241 ± 18 kJ/mol, for 10 and 50 nm-sized particles, respectively) in a higher temperature range (1100–1400 °C) using the same technique.[16]

The above activation energy for onset coarsening–coalescence of the nano- and micron-sized Co_3O_4 particles concerns the surface diffusion and mobility of the particles to form cylindrical pores and has nothing to do with the transformation from the precedent phases, i.e. $Co(OH)_2$ and CoO, respectively. This is analogous to the coarsening and repacking of other oxide powders such as Y_2O_3

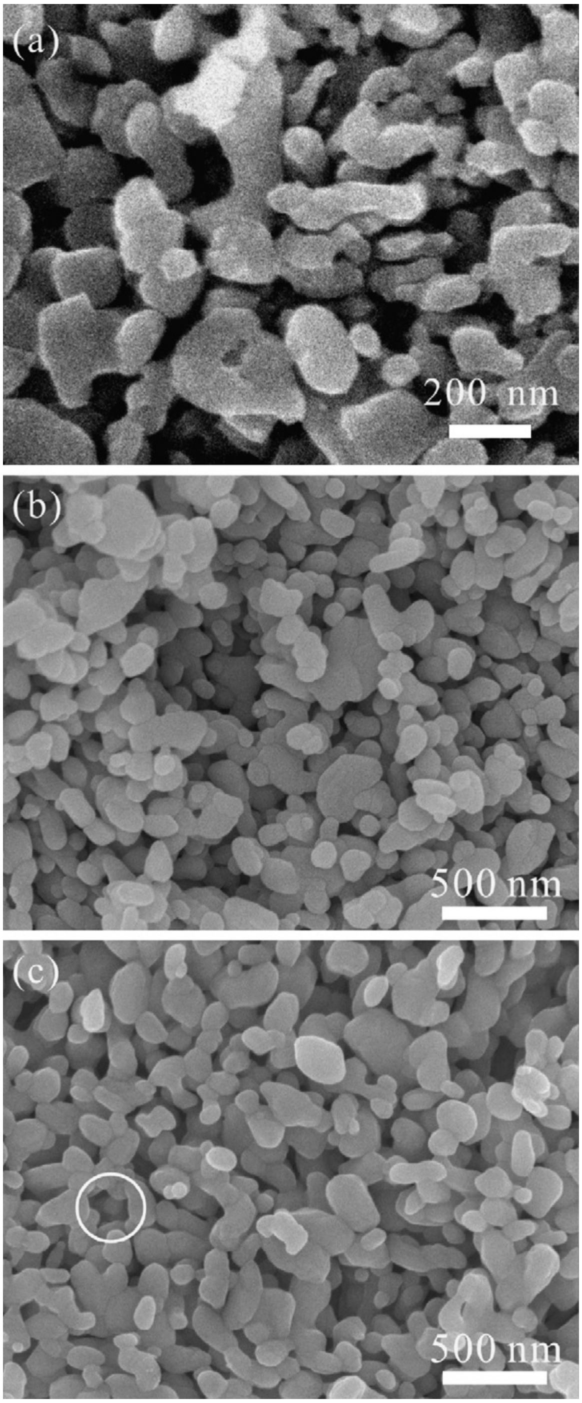

Fig. 9. Representative SEM images of micron-sized powders: (a) dry pressed green body, (b) and (c) subjected to sintering at 700 °C for 52 and 60 min, respectively to show repacking of the coarsened particles (circle) in (c).

and CeO_2,[23] and γ-Al_2O_3[16] in the onset sintering stage. The activation energy being lower may imply a more excited surface state for the nm-sized particles to coarsen-coalesce readily, although a later sintering process could also be involved as indicated by appreciable shrinkage of the nanosized sample heated at 800 °C for 4 min. Further sintering of the Co_3O_4 particles would involve grain boundary diffusion, pipe diffusion along dislocations or even lattice diffusion with an activation energy as high as 163 kJ/mol for the analogue CoO powder.[24] The Co_3O_4 would transform to CoO above 900 °C in open air conditions[25] to dominate the sintering behavior, such as that conducted at 1000 °C in this study for micron-sized particles.

It should be noted that the hexagonal plate-like shape of the nanosize Co_3O_4 particles derived from $Co(OH)_2$ following the epitaxial relationship, i.e. $[0\,0\,0\,1]_H//[1\,1\,1]_S//[0\,0\,0\,1]_{Co}$; $(1\,0\,\bar{1}\,0)_H//(\bar{1}\,\bar{1}\,2)_S//(\bar{1}\,\bar{1}\,2\,0)_{Co}$ as mentioned, could facilitate $\{1\,1\,1\}$ and $\{2\,1\,1\}$-specific coalescence of the impinged particles in the onset coarsening–repacking stage. The metallic cobalt that appears in vacuum during TEM observations does not occur in the present isothermal heating experiments because bulk CoO and Co_3O_4 are stable above and below 900 °C, respectively in the open air condition as mentioned. The cubo-octahedral meso-

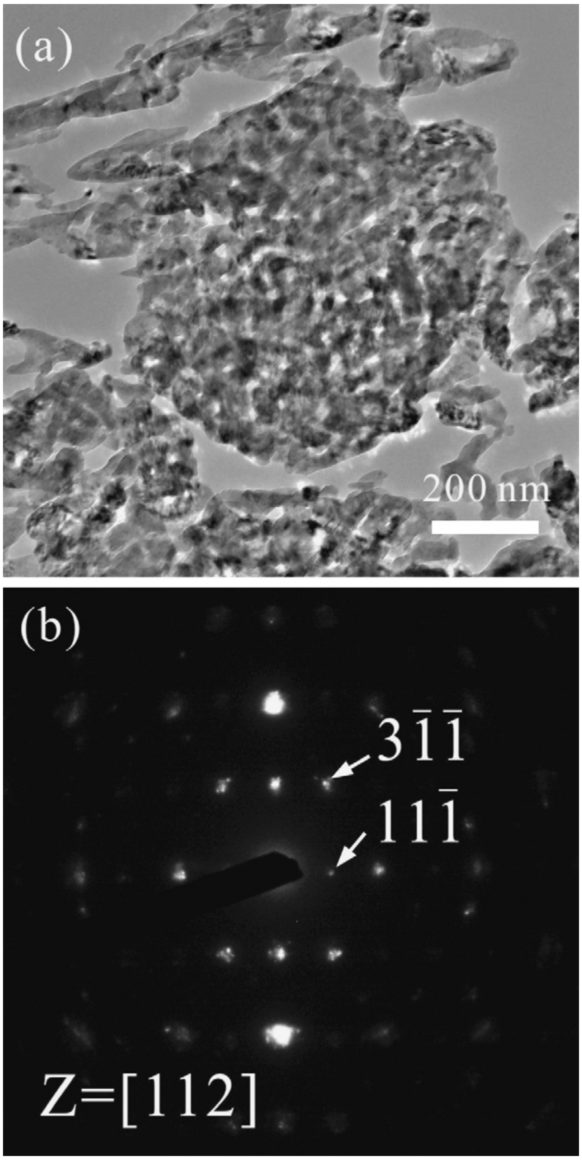

Fig. 10. (a) TEM BFI of the coarsened and coalesced Co_3O_4 plates with significantly coarsened/coalesced mesopores after firing at 600 °C for 10 min. (b) SAED pattern of such a plate as large as 800 nm in size nearly in top view in (a).

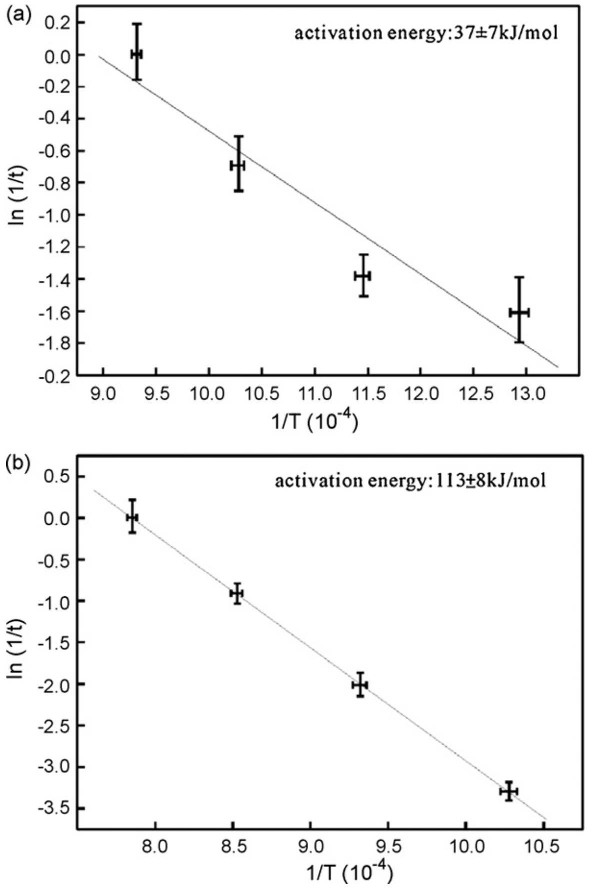

Fig. 11. Arrhenius plots of the logarithmic reciprocal time ($t_{0.7}$ and $t_{0.3}$ in min) against reciprocal temperature (in Kelvin) for specific surface area decrease by 70% and 30% from the dry pressed Co_3O_4 powders of (a) nanometer size and (b) micrometer size, respectively.

pores due to decomposition of $Co(OH)_2$ as manifested by in situ TEM observations could also migrate and coalesce to form cylindrical pores. In later stage when the particles became too larger in size to move, surface diffusion would be dominating to change the cylindrical pores into truncated pores. As for the micronsize Co_3O_4 particles with nearly equant shape after the CoO precursor, their coarsening and repacking would be rather isotropic to form cylindrical pores until grain boundary diffusion became important for further sintering.

4.3. Implications for the phase behavior of Co_3O_4 in a dynamic process

Laser ablation condensation is an effective method of producing cobalt oxide nanoparticles more or less in agglomeration and coalescence due to the considerable associated heating effect.[14] Laser ablation on Co target typically caused the condensation of $Co_{1-x}O$ nanocrystals which are in random orientation and partially oxidized as $Co_{3-\delta}O_4$ spinel.[14] Such nanocondensates are cubo-octahedral in shape and tend to have cube faces in parallel when agglomerated in a close packed manner by coalescence of the condensates involving Brownian motion/rotation of the nanoparticles under the influence of radiant heating during pulsed laser ablation.[14] Radiant heating was suggested to be up to about 1000 °C in view of the change of NCA into a close packed manner analogous to the case of TiO_2 condensates produced by gas evaporation method[15] or laser ablation condensation process.[26,27] The present isothermal static heating results coupled with BET/BJH measurements further indicated that the temperature could be as low as 500 °C for effective coarsening and coalescence of nanosize Co_3O_4 particles with a prolonged dwelling time.

5. Conclusions

1. BET/BJH adsorption–desorption hysteresis isotherms of Co_3O_4 nanoplates and equi-axed powders micrometers in size were used satisfactorily to determine an incubation time for the formation of cylindrical pores and accompanied drastic change of specific surface area as a characteristic of an onset coarsening–coalescence event.
2. In the temperature range of 500–1000 °C, the apparent activation energy for the onset coarsening–coalescence process was determined as 37 ± 7 and 113 ± 8 kJ/mol, for the nanoplates and micron-sized powders, respectively indicating easier surface diffusion for the former despite the more rapid Co_3O_4 transformation into CoO above 900 °C.
3. The surface area reduction process of the nanoplates with a hexagonal pseudomorph after the precursor $Co(OH)_2$ phase was found to be controlled by (1 1 1)-specific coalescence besides a coarsening–repacking process common to that for the equi-axed particles.

4 The present static heating results of onset coarsening–coalescence of the Co_3O_4 (below 900 °C) or CoO particles (above 900 °C) support our previous supposition that such particles in an assembly of nanochain aggregates are able to coalesce and/or sinter into a close packed manner by radiant heating below 1000 °C in a dynamic laser ablation process.

Acknowledgments

We thank Drs. C.N. Huang and S.Y. Chen for helpful discussion on the coalescence of CoO and Co_3O_4 nanoparticles in a dynamic laser ablation condensation process and an anonymous referee for helpful comments. Supported by Center for Nanoscience and Nanotechnology at NSYSU and National Science Council, Taiwan, ROC.

Appendix A.

Types of (a) physisorption isotherms and (b) adsorption–desorption hysteresis loops after Sing et al.[20]

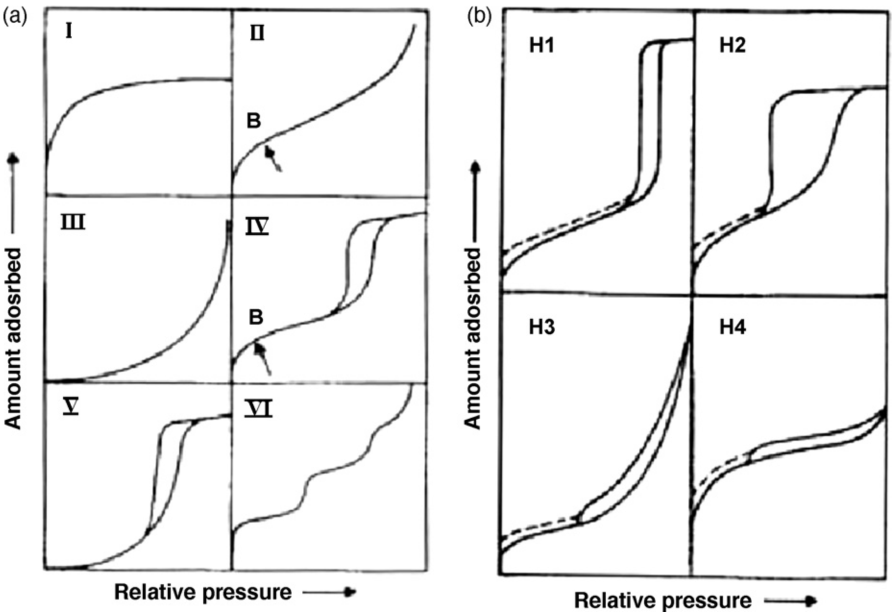

Appendix B.

Observed rate curves in terms of the reduction of specific surface area ($\Delta S/S_0$, where S_0 is the initial quantity) versus time for nanosize $Co(OH)_2$ derived Co_3O_4 powder at specified temperatures (cf. Table 1). The time $t_{0.7}$, i.e. with 70% reduction of specific surface area as denoted by dashed line is used for activation energy estimation, respectively for the nanosized powders.

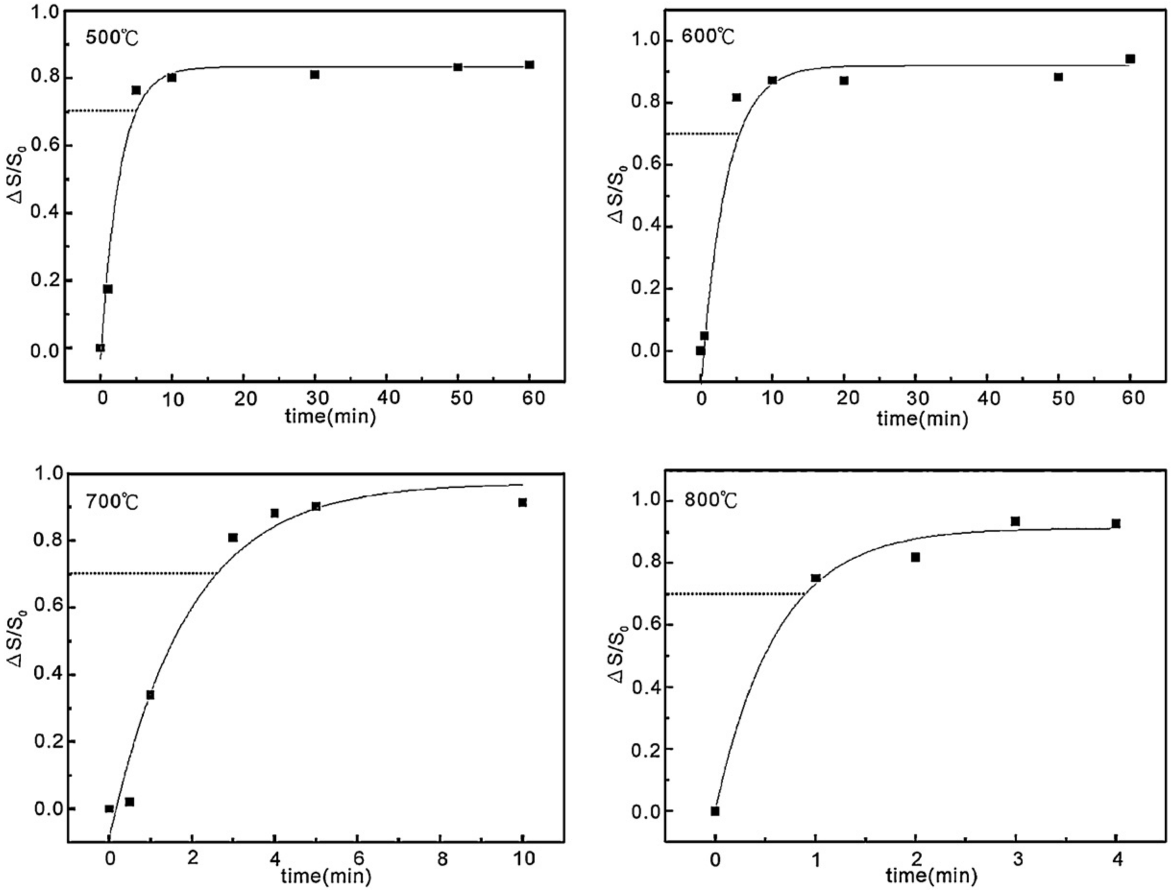

Appendix C.

Observed rate curves in terms of the reduction of specific surface area ($\Delta S/S_0$, where S_0 is the initial quantity) versus time for CoO-derived Co_3O_4 micron powders at specified temperatures (cf. Table 2). The time $t_{0.3}$, i.e. with 30% reduction of specific surface area as denoted by dashed line is used for activation energy estimation, respectively for the micron-sized powders.

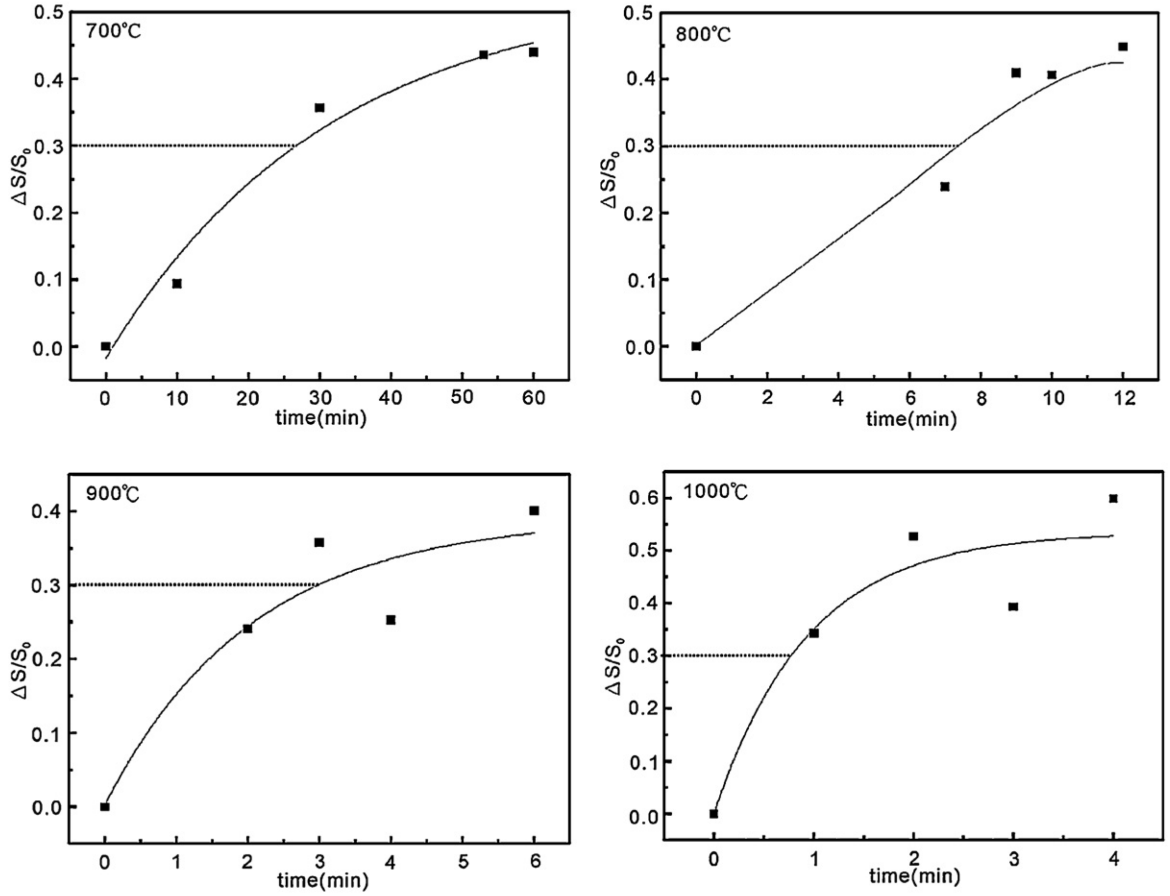

References

1. Haber, J., Crystallography of catalyst types. In *Catalysis Science and Technology, vol. 2*, ed. J. R. Anderson and M. Boudart. Springer-Verlag, Berlin, 1981, pp. 1–95.
2. Bond, G. C., *Heterogeneous Catalysis Principles and Applications*. Oxford University Press, Oxford, 1992, pp. 1–176.
3. Lee, W. H. and Shen, P., Interdiffusion induced defect microstructures of $Co_{1-x}O$ near confined zirconia particles. *Micron*, 2002, **33**, 555–559.
4. Lee, W. H. and Shen, P., $Co_{3-\delta}O_4$ paracrystal: 3-D assembly of nano-size defect clusters in spinel lattice. *J. Solid State Chem.*, 2004, **177**, 101–108.
5. Li, M. Y. and Shen, P., On the nucleation and paracrystal interspacing of Zr-doped $Co_{3-\delta}O_4$. *Mater. Sci. Eng. B*, 2004, **111**, 82–89.
6. Tsai, T. M., Yang, K. C. and Shen, P., Defect clusters and precipitation/oxidation of MgO–$Co_{1-x}O$ solid solution. *J. Solid State Chem.*, 2004, **177**, 3301–3309.
7. Lee, W. H. and Shen, P., Reorientation of intra- and intergranular particles in sintered Y-PSZ/$Co_{1-x}O$ composites. *Mater. Sci. Eng. A*, 2002, **338**, 253–258.
8. Li, M. Y., Shen, P. and Hwang, S. L., Oxidation–decomposition facilitated reorientation of nanoparticles in reactively sintered $(Ni_{0.33}Co_{0.67})_{1-\delta}O$ polycrystals. *Mater. Sci. Eng. A*, 2003, **343**, 227–234.
9. Wang, J. Y. and Shen, P., (1 1 1)-Specific reorientation and shape change of $Co_{1-x}O$ particles within CaO grains. *Mater. Sci. Eng. A*, 2003, **359**, 192–197.
10. Lee, W. H. and Shen, P., Thermal-mismatch induced cleaving and spontaneous healing of zirconia dispersed $Co_{1-x}O$. *Mater. Sci. Eng. A*, 2002, **332**, 262–269.
11. Li, M. Y., Shen, P. and Hwang, S. L., Transformation-enabled cleaving and healing in zirconia dispersed $Co_{1-x}O$. *Mater. Sci. Eng. A*, 2004, **386**, 104–111.
12. Huang, C. N., Shen, P. and Hsieh, K. Y., On the surface morphology of solution annealed $Co_{1-x}O$–MgO—effects of directional dislocation exposure and $Co_{1-x}O$ condensation. *J. Eur. Ceram. Soc.*, 2007, **27**, 4685–4695.
13. Ji, J. Y., Shen, P., Chen, J. C., Kao, F. J., Huang, S. L. and Lo, C. Y., On the deposition of $Cr_{3-\delta}O_4$ spinel particles upon laser heated pedestal growth of Cr:YAG fiber. *J. Cryst. Growth*, 2005, **282**, 343–352.
14. Huang, C. N., Chen, S. Y., Tsai, M. H. and Shen, P., Laser ablation condensation and phase change of $Ni_{1-x}Co_xO$ nanoparticles. *J. Cryst. Growth*, 2007, **305**, 285–295.
15. Jang, H. D. and Friedlander, S. K., Restructuring of chain aggregates of titania nanoparticles in the gas phase. *Aerosol Sci. Technol.*, 1998, **29**, 81–91.
16. Liu, I. L. and Shen, P., Onset coarsening/coalescence kinetics of γ-type related Al_2O_3 nanoparticles: implications to their assembly in a laser ablation process. *J. Eur. Ceram. Soc.*, 2009, **29**, 2235–2248.
17. Pan, C., Chen, S. Y. and Shen, P., Laser ablation condensation, coalescence and phase change of dense γ-Al_2O_3 particles. *J. Phys. Chem. B*, 2006, **110**, 24340–24345.
18. Brunauer, S., Emmett, P. H. and Teller, E., Adsorption of gases in multimolecular layers. *J. Am. Chem. Soc.*, 1938, **60**, 309–319.

19. Barrett, E. P., Joyner, L. G. and Halenda, P. P., The determination of pore volume and area distribution in porous substances. I. Computations from nitrogen isotherms. *J. Am. Chem. Soc.*, 1951, **73**, 373–380.
20. Sing, K. S. W., Everett, D. H., Haul, R. A. W., Moscou, L., Pierotti, R. A., Rouquerol, J. and Siemieniewska, T., Reporting physisorption data for gas/solid systems with special reference to the determination of surface area and porosity. *Pure Appl. Chem.*, 1985, **57**, 603–619.
21. Platero, E. E., Coluccia, S. and Zecchina, A., CO and NO adsorption on NiO: a spectroscopic investigation. *Langmuir*, 1985, **1**, 407–414.
22. Jiang, Y., Wu, Y., Xie, B., Xie, Y. and Qian, Y., Moderate temperature synthesis of nanocrystalline Co_3O_4 via gel hydrothermal oxidation. *Mater. Chem. Phys.*, 2002, **74**, 234–237.
23. Chen, P. L. and Chen, I. W., Sintering of fine oxide powders. *J. Am. Ceram. Soc.*, 1997, **80**, 637–645.
24. Chen, W. K., Peterson, N. L. and Reeves, W. T., Isotope effect for cation self-diffusion in CoO crystals. *Phys. Rev.*, 1969, **186**, 887–891.
25. Oku, M. and Sato, Y., In-situ X-ray photoelectron spectroscopic study of the reversible phase transition between CoO and Co_3O_4 in oxygen of 10^{-3} Pa. *Appl. Surf. Sci.*, 1992, **55**, 37–41.
26. Tsai, M. H., M.S. Thesis. National Sun Yat-sen University, Taiwan, 2002.
27. Tsai, M. H., Chen, S. Y. and Shen, P., Imperfect oriented attachment: accretion and defect generation of nanosize rutile condensates. *Nano Lett.*, 2004, **4**, 1197–1201.